Zeitschrift: Helvetica Physica Acta
Band: 45 (1972)
Heft: 3

Artikel: Solid state reactions and defects in doped Verneuil sapphire. III, Systems -Al2O3:Fe, -Al2O3:Ti and -Al2O3:(Fe, Ti)
Autor: Eigenmann, Kaspar / Kurtz, Karl / Günthard, Hs.H.
DOI: https://doi.org/10.5169/seals-114393

Helvetica Physica Acta
Vol. 45, 1972

Birkhäuser Verlag Basel

Solid State Reactions and Defects in Doped Verneuil Sapphire

III[1]. Systems α-Al_2O_3: Fe, α-Al_2O_3: Ti and α-Al_2O_3: (Fe, Ti)

by **Kaspar Eigenmann[2]**, **Karl Kurtz[2]** and **Hs. H. Günthard**

Swiss Federal Institute of Technology, Laboratory of Physical Chemistry, Zurich, Switzerland

(27. VIII. 71)

Abstract. Extending earlier work on Ni and Co doped sapphire to Ti, Fe and doubly doped (Fe, Ti) sapphire the phenomenon of non additive color of multiply doped corundum was given special attention. Since in all these cases Verneuil grown crystals show inhomogeneous dopant distribution, local concentrations were determined by electron microprobe analysis calibrated by neutron activation analysis. Polarized and high resolution UV-VIS spectra, polarized IR and quantitative ESR spectra of the doped crystals in the untreated state and after oxidation by O_2 and reduction by H_2 at 1500 °C are given. Information derived therefrom shows Ti to be present as Ti^{+3} and Ti^{+4}, Fe as Fe^{+2} and Fe^{+3} and (Fe, Ti) as $(Fe, Ti)^{+6}$ and $(Fe, Ti)^{+7}$ in the reduced state and oxidized state respectively. In the reduced state hydrogen is shown by polarized infrared spectra and isotopic shifts to occupy an interstitial site between two O^{-2} ions of the larger oxygen triangles on (001) planes. For assignment of the UV-VIS bands near 385 and 450 nm of α-Al_2O_3: Fe^{+3} extended crystal field calculations were carried out based on a point charge lattice, using all 3 d^n electron configurations of Ti^{+3} and Fe^{+3} and Hartree-Fock atomic orbitals for free ions. In order to obtain acceptable agreement between observed and calculated spectra the quantity $\langle r^4 \rangle$ is considered as a fitting parameter, leading to considerably higher $\langle r^4 \rangle$ values for both Ti^{+3} and Fe^{+3}. Under this assumption an assignment for the α-Al_2O_3: Fe^{+3} spectrum compatible with the observed polarization and high resolution UV-VIS data may be given. The characteristic and nonadditive spectrum of α-Al_2O_3: (Fe, Ti) in the reduced state is shown by various arguments to originate from a biparticle $(Fe, Ti)^{+6}$. Finally thermodynamic data for redox reactions and relatively detailed models for the substituted ions in different oxidation states are given.

1. Introduction

Optical and magnetic properties of transition metal ions substituted into the α-Al_2O_3 structure have been subject to intensive study. Optical spectra of ions of the iron series substituted on Al^{+3} sites up to 1962 have been discussed by McClure [1]. Geschwind and Remeika [2] published extensive analyses of ESR spectra of Ni^{+3}, Ni^{+2}, Co^{+3}, V^{+3} in sapphire grown from oxide fluxes. In some of these systems valence

---

[1]) For paper I, c.f. Ref. [14], for paper II, c.f. Ref. [36].

[2]) Work extracted in part from Ph. D. theses of Kaspar Eigenmann [39] and Karl Kurtz [19].

states are difficult to establish. Several investigations have been directed towards the study of changes of valence states of substituted ions and the accompanying variations of optical and ESR spectra. Any such change must involve a charge compensating process which may involve either impurities or charge variations of other constituents of the α-Al_2O_3 structure. The same principle of charge compensation applies to growth of doped crystals by either growth method. As a consequence substitution of Me^{+2} ions on Al^{+3} sites implies either defects or vacancies in the Al_2O_3 structure or charge compensation by interstitial or substitutional impurity ions.

In most cases ESR, fluorescence or/and optical spectra have been used to identify valence states of transition metal ions. Sturge [3] observed fluorescence of V^{+2}, after irradiation of α-Al_2O_3:V^{+3} with Co^{60} radiation. Similarly Lambe and Kikuchi [4] were able to detect the ESR spectra of α-Al_2O_3:V^{+2}, α-Al_2O_3:V^{+4} in α-Al_2O_3:V^{+3} irradiated by 50 kV X-rays. By admixture of metal nitrides in the Verneuil growth process, Hoskin [5] reported the ESR spectrum of Cr^{+4} assuming charge compensation by substitution of N^{-3} for O^{-2}. Geschwind [6] et al. used Mg^{+2} for charge compensation in α-Al_2O_3:Mn^{+4} whose identity was established by ESR, thermoluminescence and fluorescence spectra. Mg^{+2} also proved efficient for substitution of Co^{+4} in sapphire grown from PbO-B_2O_3 melts [7]. Müller et al. [8] were the first to produce reversible valence changes of α-Al_2O_3:Ni^{+3} and α-Al_2O_3:Co^{+3} by high temperature reactions according to

$$M^{+3} + \frac{1}{2} H_2 \rightarrow M^{+2} + H^+ , \qquad (1')$$

$$H^+ + 2O^{-2} \rightarrow OHO^{-3} , \qquad (1'')$$

using gaseous H_2 and O_2 respectively. The existence of the hydrogen was demonstrated by IR absorption bands in the 3 μ region in the reduced state of the doped crystals. In these systems therefore the charge compensating particle involved in the valence state change of the transition metal ion may be identified. Recently these results were confirmed by Hauffe et al. [9] who tried to give a more detailed model for the diffusion processes involved in the redox process.

Several workers have studied the systems investigated in this paper, i.e. α-Al_2O_3:Fe, α-Al_2O_3:Ti and α-Al_2O_3:(Fe, Ti). ESR spectra of α-Al_2O_3:Fe^{+3} have been measured by Kornienko et al. [10], who also published ESR data of α-Al_2O_3:Ti^{+3}.

Optical spectra of Fe- and Ti-doped sapphire were discussed by McClure [1]. Recently Lehmann et al. [11] reported optical spectra of natural blue sapphire. Obviously some of the crystals doped with several transition metal ions exhibit non-additive spectra. A rather extended series of non additive UV and VIS spectra of multiply doped sapphire have been reported by S. V. Grum-Grschumaulo [12] and by Keig [13].

In this work a detailed study of the redox processes of Fe, Ti and (Fe, Ti) doped sapphire grown by the Verneuil process is given. Since distribution of dopants in such crystals is non uniform considerable effort has been made to obtain reliable information about concentration profiles of Ti and Fe in the crystals by instrumental neutron activation and electron microprobe analysis. From analytical data correlation of absorption spectra with concentrations of dopants is derived. It is shown that heat treatments near 1550 °C in either H_2, O_2 or vacuum involves irreversible processes in

the first step, similar but not identical to those observed for defect laser rubies grown by Verneuil process [14]. Succeeding redox treatments involve changes of the valence states in Fe, Ti and (Fe, Ti) doped sapphire which are identified by IR, VIS-UV and ESR spectra. Intensity measurements of ESR spectra are used to derive information on valence states and degree of reduction or oxidation respectively produced by treatment in hot gas atmospheres.

Arguments based on empirical data and extended crystal field calculations are presented for assignment of the crystal field absorption spectra of Fe^{+3} and (Fe, Ti) doped sapphire. Using thermodynamic considerations rather detailed models are given for the structure of the defects involving the transition metal ions and for the charge compensation processes accompanying high temperature redox reactions. Evidence is presented for the existence of (Fe, Ti) pairs to which the characteristic blue color of (Fe, Ti) doped sapphire is correlated.

2. Experimental

Materials

In this study doped sapphire samples grown by the Verneuil process were used exclusively. Fe doped crystals were grown with 60° orientation, whereas Ti and (Fe, Ti) doped samples were grown with 90° orientation. Dopant concentrations in the raw material used in the Verneuil process (nominal) and single crystals obtained from it (actual) are listed in Table 1. Actual concentrations were determined by electron microprobe (EMP) measurements and by instrumental neutron activation analysis (INAA). Details about analytical procedures, accuracy and correlation between the two methods are published elsewhere [15]. The dopants, in particular Ti and (Fe, Ti), were found to be distributed quite inhomogeneously. Therefore considerable care has been applied in obtaining spectroscopic samples with nearly homogeneous distribution from Verneuil boules.

Table 1
Dopant Concentration in Raw Material and Verneuil Sapphire Crystals.

Crystal	Raw Material		Verneuil Crystal[a])	
	Fe	Ti	Fe	Ti
α-Al_2O_3: Fe	2000 ppm	–	75 ppm	–
α-Al_2O_3: Ti	–	600 ppm	–	350–600 ppm
α-Al_2O_3: (Fe, Ti)	8800 ppm	600 ppm	250–1000 ppm	60–350 ppm

[a]) In case of inhomogeneous crystals the range of concentrations measured in the center and at the periphery are given.

For ESR samples cylindrical rods of 1.5 mm diameter and 10–20 mm length were cut from the boules with the crystallographic *c* axes parallel to the cylinder axis. α-Al_2O_3:Fe samples were prepared from the boules center, whereas for α-Al_2O_3:Ti and α-Al_2O_3:(Fe, Ti) samples from both the central and the peripherical zone were

taken. Samples for optical measurements in the infrared (IR), visible (VIS) and ultraviolet (UV) region and for measurement of the concentration profiles were plane parallel plates of 1–2 cm diameter and 0.1–8 mm thickness, cut and polished with the face parallel to the *c* axis. For high resolution and Zeeman measurements of (Fe, Ti) doped α-Al_2O_3 plates of $8\times1\times3.7$ mm^3 (*c*-axis parallel to 3.7 mm edge) were cut from the outer zones of raw boules. They were polished and assembled to a prismatic sample of $8\times8\times3.7$ mm^3.

High Temperature Reduction Oxidation Treatment

For high temperature treatments up to 1650 °C two furnace systems have been used both allowing treatment of samples in a flow system with either H_2 or O_2 atmosphere of approximately 1 at pressure or in vacuo; flow rates were approx. 60 cm^3/min. Samples for optical measurements were heated by a SOLO-furnace [16], model HRO 3754 KS, in sintered alumina tubes (99.5% Al_2O_3, 25 mm i. diam.).

The tubes were ground at both ends to accept water colled O-Ring seals for connection to flow or vacuum systems. ESR samples were subject to high temperature treatments in a Metals Research [17] furnace, model PCA 10, equipped with its own flow system and accessories for pyrometric temperature measurements. It should be pointed out that use of a flow system is essential for precise control of the gas atmosphere. Permeation of gases through the walls of the alumina tube at temperatures above 1000 °C proved to introduce significant contamination if a stationary gas atmosphere was applied. Furthermore it should be mentioned that even under flow conditions noticeable transport of dopant material from the samples into the alumina tubes was observed.

Optical Spectra and Zeeman Measurements

Measurement of VIS-UV spectra at low resolving power were made with a Beckman model DK2 spectrophotometer, equipped with a set-up for polarization measurements and exact setting of samples [18]. By use of circular apertures down to 1 mm diameter in both sample and reference beams nearly local absorption spectra could be obtained reproducibly. Owing to birefrigence and anisotropy reproducibility of measurements proved to depend critically on precise setting and orientation of the samples in the beams. LHe and LN_2 temperature spectra were determined with a cryogenic cell of our own design fitting in the sample compartment of the DK2. For study of the complex and very weak band group near 385 nm a high resolution Zeeman set-up scetched in Figure 1 was built [19]. The sample was mounted in a LHe cryostate of our own design, which fitted directly into the gap of a magnet yielding a max field of 12 kGauss at a 1″ gap. For the low noise detector system a home made preamplifier phase sensitive detector se-tup with the reference signal taken from a photodiode controlled by a mechanical chopper was used. All data were collected by means of a data acquisition system described earlier [20]. Owing to the weak absorption of the 385 nm bands samples with relatively low transmittance (typically 1%) in the 385 nm region were used. This on the other hand necessitated a slit width of ~ 9 cm^{-1} yielding signal to noise ratios of 5 at time constants of 1–3 s. For careful control of drifts the measurement of spectra and Zeeman effect was made by a

sequence of field on-field off measurements at 1.5 cm^{-1} intervals. The digitized data were analyzed by a line shape program including a quadratic base line into a set of Lorentzian shapes with a preselected number of bands.

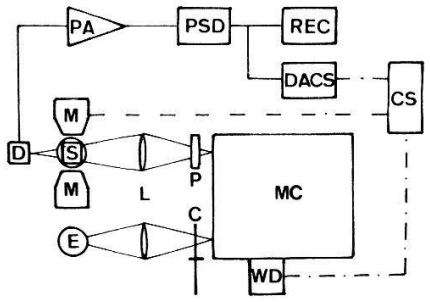

Figure 1
Experimental Set-up for Measurement of spectra and the optical Zeeman Effect.

Legend:

E	Light source (OSRAM type 64625)
MC	Monochromator (SPEX-II)
L	CaF_2 lenses
P	Polarizer (Polaroid KN 36)
S	Sample mounted in cryostate
M	Magnet (MAGNION type UFS)
D	PMT detector (RCA1P21)
PA	Preamplifier
PSD	Phase Sensitive Detector
REC	Recorder
DACS	Data Acquisition System
CS	Control System
WD	Wavelength drive
C	Chopper

Infrared Spectra

The measurements of infrared absorption spectra were carried out on a Perkin Elmer 225 instrument equipped with polarization facilities. Because of the large beam cross section relative to the sample size masks of 2–8 mm diam. were used.

ESR Spectroscopy

All measurements at room temperature were carried out on a *K* band super heterodyne spectrometer, whose description is given elsewhere [21]. Magnetic fields were measured with a self locking proton resonance magnetometer [22]. Both ESR signal and magnetic field measurements were collected with a digital data acquisition system [20] allowing processing of data by punched cards.

For quantitative measurements of ESR signal strength a special set-up was constructed following ideas proposed by D. S. Thompson [23]. By this procedure the ESR signal strength of a reference sample and the sample under investigation were measured by nearly the same conditions in the ESR spectrometer, thereby avoiding exact resettability of *rf* field and electronic amplification by comparison of reference and sample signal. The actual set-up used in this work is shown in Figure 2. As a reference sample a ruby rod of 1 mm diameter and 10 mm length, with crystallographic *c*-axis perpendicular to the rod axis, was positioned with a KelF holder from below in the lower half of the cavity (16.2 mm diameter, 16 mm height). In a similar manner the sample cylinder was positioned from above with a KelF holder connected to a goniometer head. Both crystals were held coaxially for all positions of the sample crystal by means of the ruby holder. For relative signal strength measurement the ruby sample was rotated until its signal appeared near to the sample's signal, but not overlapping it. For α-Al_2O_3:Fe^{+3}, one of whose signals at 23.8 GHz appeared near

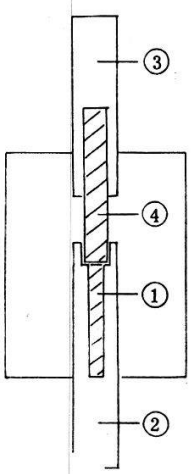

Figure 2
K Band ESR Cavity for quantitative ESR Signal Strength Measurement
Legend: 1 Cylindrical Ruby reference
2 KelF holder
3 KelF holder
4 Sample

9312 Gauss with $c \perp H$ orientation, a ruby orientation with $\measuredangle (c, H_0) = 11°$ was used, producing a α-Al_2O_3:Cr^{+3} line near 8560 Gauss. In order to determine the α-Al_2O_3:Fe^{+3} signal quantitatively both signals were recorded digitally in the same setting of the K band spectrometer by the same magnetic field sweep. Usually this measurement was repeated several (5–10) times. The digitalized signals were analysed into derivatives of Lorentzian or Gaussian lines by a least square fit. Either a linear or quadratic base line was included in the fitting process. The latter provided the parameters y'_m, H_0 and ΔH_{pp} [24] for each line, from which the integrated intensity was obtained by

$$A = \left(\frac{2\pi}{\sqrt{3}}\right) y'_m \, \Delta H_{pp}^2 \quad \text{or} \quad A = \sqrt{2\pi e}\, y'_m \, (0.5\, \Delta H_{pp})^2 \,. \tag{2}$$

Comparison of quality of the fit by Lorentzian or Gaussian line shape was made by comparison of the residual sum of squares by the F-test, i.e.

$$s^2 = \sum_{i=1}^{M} \frac{\left(Y'(H_i) - y'(H_i)\right)^2}{M - N} \,,$$

where

$Y'(H_i)$: calculated signal at H_i
$y'(H_i)$: measured signal at H_i
H_i: magnetic field
M: number of measurements
N: number of parameters.

Since in this work the Fe^{+3} signal strength of particular samples had to be measured several times after successive heat treatments, the errors introduced through resetting of the sample in the cavity were of special interest. This error obviously is relevant for conclusions to be drawn from ESR signal strength measurement and from the effects of high temperature reactions on Fe^{+3} concentration. Table 2 gives information about typical resettability errors. It may be commented upon as follows:

(i) Within a setting the parameters ΔH_{pp} and H_0 of the α-Al_2O_3:Cr^{+3} line are reproducible to high precision, whereas for α-Al_2O_3:Fe^{+3} the resonance field H_0 is highly reproducible but not the line width parameter (5% rms deviation in the second setting).

(ii) Between the settings the resonance fields are reproducible to approx. three times the rms deviation within settings. For α-Al_2O_3:Cr^{+3} ΔH_{pp} is highly reproducible (within one rms deviation within settings), for α-Al_2O_3:Fe^{+3} however the rms deviation of ΔH_{pp} is approx. 5%.

(iii) Reproducibility of the Fe^{+3} concentration between settings amounts to approx. 2%, though according to the errors of ΔH_{pp} it could be up to 10% (cf. equation (1)). No more detailed investigation concerning this point has been made. Practically an accuracy of 5–10% for the Fe^{+3} concentration may be considered a conservative estimate.

For low temperature study of α-Al_2O_3:Ti^{+3} a X band Hilger Microspin spectrometer was used together with a LHe cryostat of our design. Magnetic field measurements were made with a self locking proton resonance magnetometer working in the 2–28 MHz range [25].

Table 2
Quantitative ESR Signal Strength Measurements. Errors of Line Shape Parameters and Fe^{+3} Concentration introduced by Sample Resetting.

Parameter[a])	1st setting (10 measurements)		2nd setting (9 measurements)	
	average	variance	average	variance
H_0 (Cr^{+3})	8660.255	0.153	8660.817	0.509
H_0 (Fe^{+3})	9312.805	0.122	9313.379	0.142
ΔH_{pp}(Cr^{+3})	13.449	0.136	13.455	0.062
ΔH_{pp}(Fe^{+3})	20.751	0.259	21.922	1.083
rel. Fe^{+3} concentr.	4.507	0.175	4.568	0.097

[a]) Fields measurements in Gauss.

3. Results

Concentration Profiles of Dopants

In Figures 3, 4 and 5 the radial concentration profiles of α-Al_2O_3:Fe, α-Al_2O_3:Ti and α-Al_2O_3:(Fe, Ti) are shown. These were obtained by electron microprobe measurements and calibrated by instrumental neutron activation analysis. In α-Al_2O_3:Fe the Fe concentration in the central part is nearly homogeneous, but increases by a factor three to five within a peripheral zone of 0.5 mm thickness. Ti doped sapphire (Fig. 4) exhibits much less homogeneous distribution monotonically increasing from the center towards the periphery by a factor of two. Sapphire doped with both Fe and Ti (Fig. 5) shows a relatively homogeneous nucleus with approx. 10 mm diameter and monotonic increase within a peripheral zone of approx. 3 mm thickness for both dopants. Both behave similarly.

The samples of this investigation have not been tested for uncontrolled impurities. A detailed study of impurities has earlier been made for rubies grown under similar conditions by the Verneuil process [14]. One can therefore assume similar impurity concentrations in both types of crystals, i.e. typically 26–56 ppm Na, 33–85 ppm Mg, 60 ppm K, 30 ppm total other transition metals.

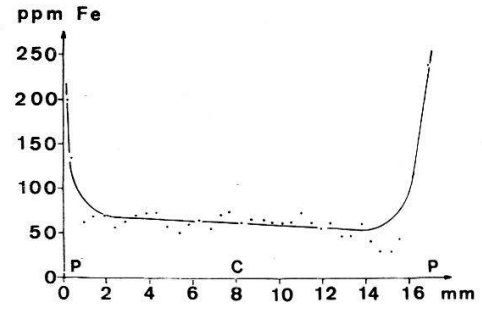

Figure 3
Radial Concentration Profile of α-Al_2O_3: Fe in Verneuil boules (Center: *C*, periphery: *P*).

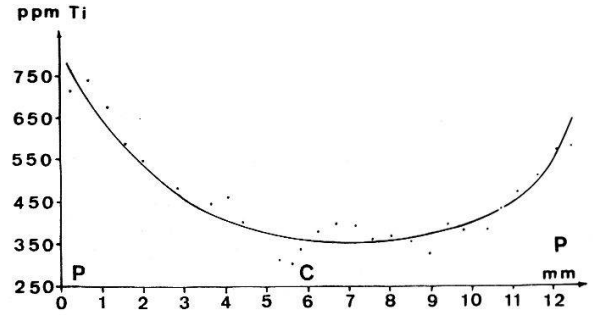

Figure 4
Radial Concentration Profile of α-Al_2O_3: Ti in Verneuil boules (Center: *C*, periphery: *P*).

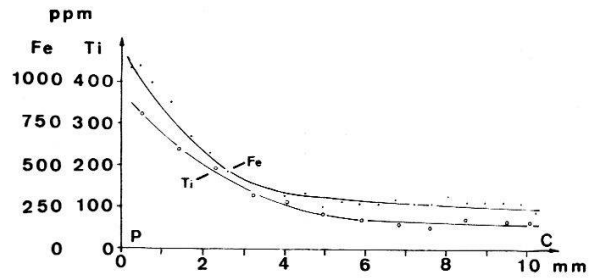

Figure 5
Radial Concentration Profiles of α-Al_2O_3: (Fe, Ti) in Verneuil boules (Center: *C*, periphery: *P*).

Optical and Infrared Spectra

Optical and infrared spectra were measured on all systems in states produced by the following general type of thermal treatment:

(i) Raw state, i.e. state of the crystals as produced by the Verneuil process.

(ii) Oxidized state, i.e. the state produced by treatment in O_2 atmosphere at temperatures between 1000 and 1550 °C from the raw state.

(iii) Reduced state, i.e. the state obtained from the raw state by treatment in H_2 at temperatures between 1000 and 1550 °C.

(iv) Oxireduced state, i.e. the state obtained by H_2 treatment from the oxidized state at temperatures between 1000 and 1550 °C.

In order to obtain information about redistribution processes of substituted ions, local optical spectra were measured in the four states, which yielded concentration profiles of the substituents.

1. α-Al_2O_3:Fe

The UV-VIS and IR spectra of this system in different states of thermal treatment are shown in Figure 6 and Figure 11 respectively. The following statements should be made:

(i) In the raw state α-Al_2O_3:Fe exhibits two absorption bands near 258 and 395 nm and no detectable absorption in the 3400–3100 cm^{-1} near IR region.

(ii) Oxidized state: Between 1100 and 1200 °C the 395 nm band disappears (cf. Fig. 6 curves 2 V–4 V), treatment at 1400 °C yields crystals of higher transparence and at 1550 °C transparency is further increased and new weak absorption bands at 392 ($\perp$), 387 ($\perp$ + ||) and 373 nm (||) appear. These bands will be discussed in more details in the next section. No change in the near infrared region is found.

(iii) Reduced state: At 1100–1200 °C the 395 nm band is removed too. Above 1200 °C the transparency decreases, but even at 1550 °C no infrared absorption was decernible.

(iv) Oxireduced state: The three bands near 385 nm disappear but only after 40 hours H_2 treatment at 1400 °C. Similarly the transparency of the material decreases after treatment above this temperature. On the other side three sharp bands appear gradually with increasing temperature in the near infrared, as is demonstrated in Figure 11a.

By measurement of the local optical absorption spectra it was found that in neither of the states were changes of the concentration profile detectable.

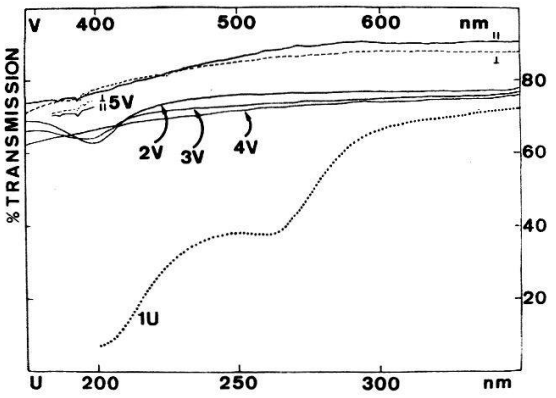

Figure 6
α-Al_2O_3: Fe UV-VIS Spectra.

Legend:

Lower Scale (UV = U): 1 U: Unpolarized UV-Spectrum of raw state.
Upper scale (VIS = V): 2 V, 3 V, 4 V: Annealing of 395 nm band by heat treatment, raw (2 V), 20 h 1100 °C (3 V), 20 h 1200 °C (4 V); 5 V ($\perp$, ||): polarized spectra of oxidized state.

2. α-Al_2O_3:Ti

UV-VIS and near IR spectra are shown in Figure 7 and Figure 11 respectively and should be commented upon as follows:

(i) In the raw state the VIS spectrum of α-Al_2O_3:Ti is characterized by absorption bands at 490 nm (||) and 550 nm ($\perp$), which are due to *d-d* transitions of α-Al_2O_3: Ti^{+3} [1]. The UV spectrum is characterized by monotonic decrease of transmission below 350 nm and one absorption band at 265 nm. With respect to the near IR spectrum the samples investigated show occasionally absorption bands of the type shown in Figure 11b.

(ii) Oxidized state: O_2 treatment above 1300 °C changes the spectra very markedly, as demonstrated by Figure 7, curve 8 V. The typical Ti^{+3} crystal field bands (490, 550 nm) are considerably reduced in intensity, but even at 1550 °C after 80 hours a pink nucleus remains. In a thin peripheral zone and in the central part these bands vanish nearly completely, as is proven by local spectra measurements with 2 mm diameter aperture, presented in Figure 9. For derivation of this information the Ti^{+3} bands at 490 and 550 nm have been subject to a line shape analysis into two Gaussian

lines and a linear base line. In Figure 9 the integrated absorption coefficients of the two bands are plotted versus the distance from the crystal plate's center yielding the radial distribution.

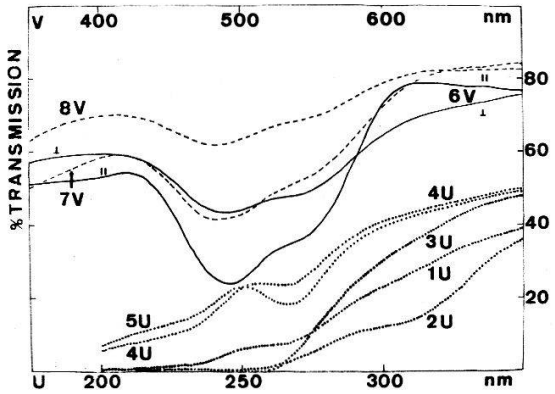

Figure 7
α-Al_2O_3: Ti UV-VIS Spectra.

Legend:

Lower scale (UV = U): 1 U, 2 U, 3 U: Oxidation of raw state, unpolarized spectra after O_2 treatment of 20 h at 1100 °C (1 U), 20 h at 1300 °C (2 U) and 80 h at 1550 °C (3 U); 4 U, 5 U: unpolarized spectra of raw state in the center (4 U) and at the periphery (5 U).

Upper scale (VIS = V): 6 V ($\perp$, $\parallel$): polarized spectra of reduced state; 7 V, 8 V: unpolarized spectra of reduced (7 V) and oxidized state (8 V).

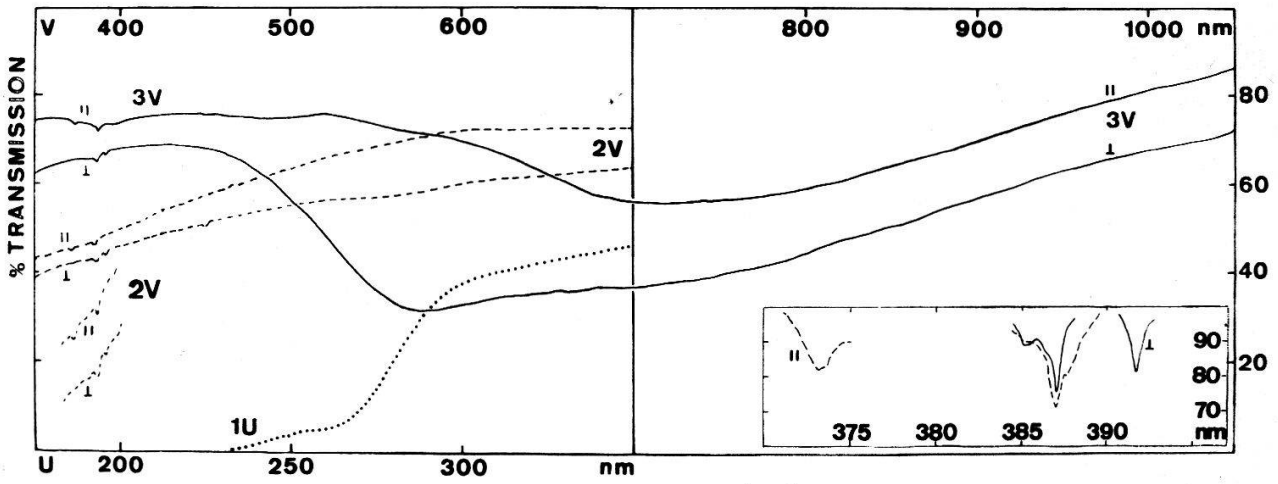

Figure 8
α-Al_2O_3: FeTi UV-VIS Spectra.

Legend:

Lower scale (UV = U): 1 U: unpolarized spectrum of raw state.

Upper scale (VIS = V): 2 V ($\perp$, $\parallel$): polarized spectra of oxidized state; 3 V ($\perp$, $\parallel$): polarized spectra of reduced state.

Inserted Figure: High resolution polarized spectra of 385 nm band group of raw state (ordinate: relative transmission).

In the UV region 1300 °C treatment produces a new band near 315 nm (Fig. 7, curve 2 U), besides the 265 nm band. At 1550 °C the 315 nm band disappears (Fig. 7, curve 3 U) and the absorption at 265 nm cannot be detected in the strong general absorption starting around 300 nm. 1400 °C treatment of α-Al_2O_3:Ti yielded gener-

ally pronounced turbidity, which excluded meaningful absorption measurements. The origin of this turbidity has not yet been investigated. All infrared bands between 3100–3400 cm^{-1} disappear above 1300 °C.

(iii) Reduced state: All spectra are very similar to spectra of the raw state. In particular the near IR bands do not change intensity upon H_2 treatment of raw crystals.

(iv) Oxireduced state: Treatment above 1300 °C yields an increase in intensity of the two Ti^{+3}-bands around 500 nm and all crystals show near IR absorptions as shown in Figure 11b.

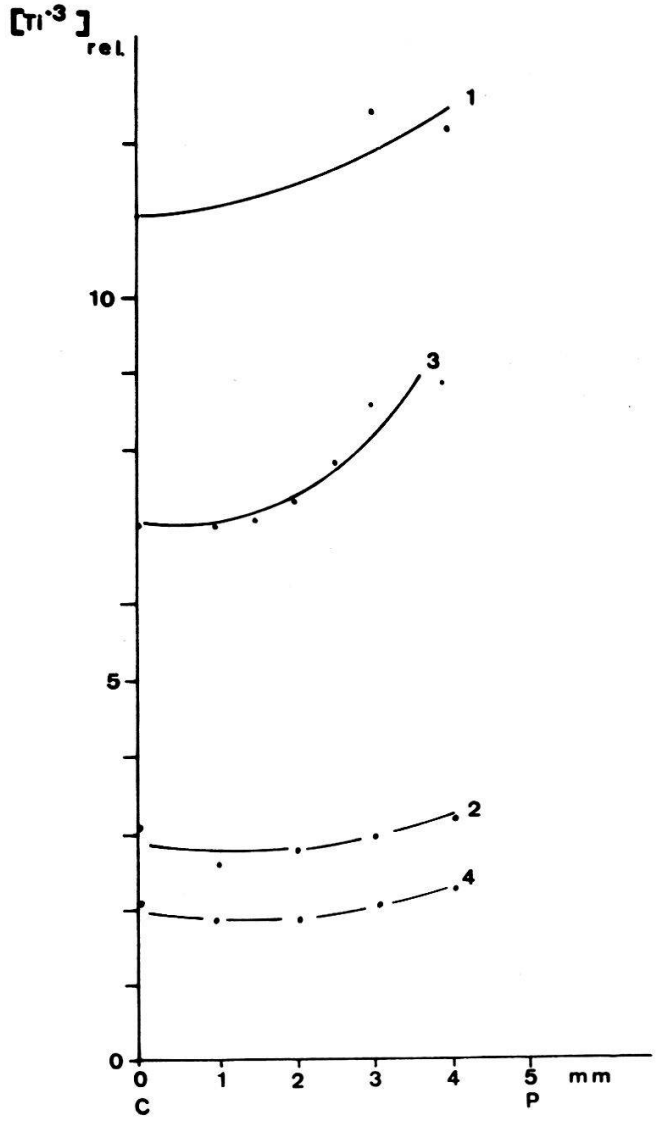

Figure 9
α-Al_2O_3: Ti; Radial dependence of Relative Ti^{+3}-Concentration on Redox Treatment [raw state (1)], oxidized from raw state (2), reduced from oxidized state (3) and oxidized from reduced state (4).

3. α-Al_2O_3: (Fe, Ti)

UV-VIS and IR spectra are shown in Figures 8 and 11. These should be complemented by the following statements, which apply to the coloured peripheral zone containing relatively high concentrations of the dopants, according to concentration profile Figure 5.

(i) Raw state: The visible spectrum is identical with that of the reduced state and is characterized by a broad absorption between 800 and 500 nm composed of at least two bands, one centered around 720 nm without pronounced polarization and one around 565 nm with perpendicular polarization. Furthermore bands at 392 ($\perp$), 387 ($\perp + \parallel$) and 373 nm ($\parallel$) occur, similar to those observed with α-Al_2O_3:Fe, but of considerably higher intensity. In the UV region the 265 nm band found in other systems occurs. In the near IR two bands near 3310 cm^{-1} and 3230 cm^{-1} could be found (Fig. 11c).

(ii) Oxidized state: Treatment in O_2 above 1400 °C yields nearly colorless crystals. The broad absorption between 500 and 800 nm nearly disappears, but the bands around 370–395 nm increase in intensity together with the appearance of a similar band at 450 nm ($\perp$). No infrared bands can be observed in this state.

(iii) Reduced state: No changes in the VIS-UV spectra can be observed, but the IR absorption between 3100–3400 cm^{-1} increase in intensity.

(iv) Oxireduced state: The VIS-UV spectra become similar to those of the raw and the reduced states above 1400 °C, whereas the near IR absorptions appear at 1100–1200 °C.

It seems that oxidation and reduction in the case of α-Al_2O_3:(Fe, Ti) is reversible. This is demonstrated in Figure 10, which shows the results of local spectra measurements with 2 mm diameter aperture. Because of the broadness of the bands in the visible the change in concentration of the absorbing species was measured by comparing the optical density at 600 nm in the different states of α-Al_2O_3:(Fe, Ti). Furthermore Figure 10 demonstrates the strong inhomogeneity of α-Al_2O_3:(Fe, Ti).

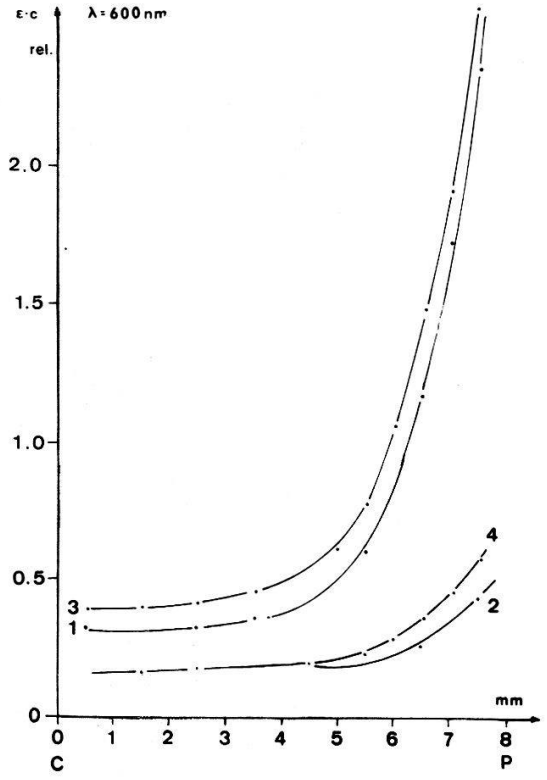

Figure 10
α-Al_2O_3: (Fe, Ti): Influence of Redox Treatment on Radial Distribution of Optical Density at 600 nm [raw state (1), oxidized from raw state (2), reduced from oxidized state (3) and oxidized from reduced state (4)].

High Resolution Optical and Zeeman Measurements of the 385 nm Bands

The band group near 385 nm as measured by the high resolution set up is shown in Figure 8 and may be commented upon as follows:

(i) At LHe temperature the 385 nm band group is found to consist of 6 polarized bands, the data of which are collected in Table 3.

(ii) Both frequencies and line width do not vary detectably between LN_2 and LHe temperature.

(iii) The central band at 25842 cm^{-1} (387 nm) consists of two components (ca. 3.4 cm^{-1} apart) with different polarization. Furthermore this band is accompanied by two further bands -60 and $+110$ cm^{-1} apart which are $\parallel$ and $\perp$ polarized.

(iv) The relatively broad absorption at 26800 cm^{-1} may either be fitted as a single band or as a super-position of two bands 40 cm^{-1} apart with the same polarization. By Fischer's F test the fit for two bands is significantly better (1% level of significance) [26].

(v) With the magnetic fields available in this work no significant Zeeman shifts or splittings were detectable. From statistical analysis of the field on-field off measurements any Zeeman shift therefore must be smaller than 7 cm^{-1}, i.e. smaller than approximately 1/4 of the band width.

Table 3
Crystal Field Spectrum of α-Al_2O_3: Fe^{+3} near 385 nm.

λ[a]	$\tilde{\nu}_i$[a]	$\Delta\tilde{\nu}_i$[a]	polarization	ε[a]	assignment[b]	
Å	cm^{-1}	cm^{-1}		l/mol cm		
3729	26817 ± 6	32 ± 11	E $\parallel$ c	1.2	$\Gamma_{1/2} + 2\,\Gamma_{3/2} + \Gamma_{5/2}$	$(T_{2(a)}, {}^4G)$
3735	26776 ± 7	30 ± 10	E $\parallel$ c	0.9		
3852	25957 ± 2	29 ± 7	E $\perp$ c	1.0		
3869	25847 ± 1	28 ± 2	E $\perp$ c	4.0	$3\,\Gamma_{1/2} + 2\,\Gamma_{3/2} + 3\,\Gamma_{5/2}$	$(T_{2(b)}, {}^4G)$
3869	25845 ± 1	31 ± 2	E $\parallel$ c	3.6	$\Gamma_{1/2} + \Gamma_{1/2}$	$(T_{2(a)}, {}^2I)$
3878	25786 ± 3	35 ± 4	E $\parallel$ c	1.4		
3917	25530 ± 1	23 ± 2	E $\perp$ c	2.7	$\Gamma_{1/2} + \Gamma_{3/2} + \Gamma_{5/2}$	$(T_{2(b)}, {}^2I)$

[a] Peak frequency in air (Å, cm^{-1}), line width and peak absorption coefficient.
[b] Notation of symmetry species of the double group C_3^*, followed by the notation of the cubic crystal field (O_h) and the free ion, where (a) and (b) denotes substates of T_2, produced by the influence of the trigonal crystal field.

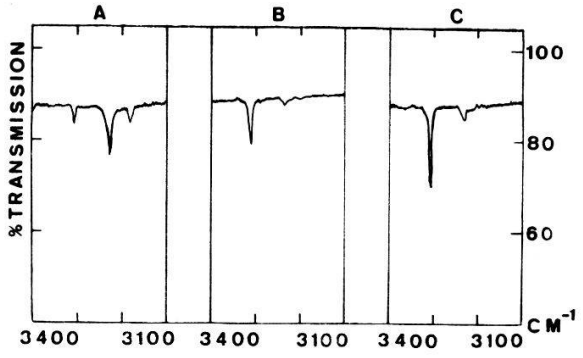

Figure 11
Near IR spectra of α-Al_2O_3: Fe (A), α-Al_2O_3: Ti (B) and α-Al_2O_3: (Fe, Ti) (C) in the reduced state.

H_2/D_2 Isotope Effects

Following the results of paper 1 for α-Al_2O_3:Ni and α-Al_2O_3:Co one expects that OHO-hydrogen bands give rise to the near IR absorptions around 3100–3400 cm^{-1}. This was proven by reduction experiments with D_2 instead of H_2 which should yield a typical isotope shift to lower frequencies. Figure 12 shows the spectrum of α-Al_2O_3: (Fe, Ti) in the near IR after treatment with H_2 at 1550 °C and the spectrum of the same crystal, treated with O_2 at 1550 °C and then reduced with D_2 (96%) for 75 hours at 1550 °C. A very marked isotope effect is observed proving the above hypothesis. In Table 4 the line position in the spectra of the H_2 and the D_2 reduced crystals are given together with the theoretical isotope shift of diatomic O–H and triatomic $D_{\infty h}$ O–H–O vibrators [27].

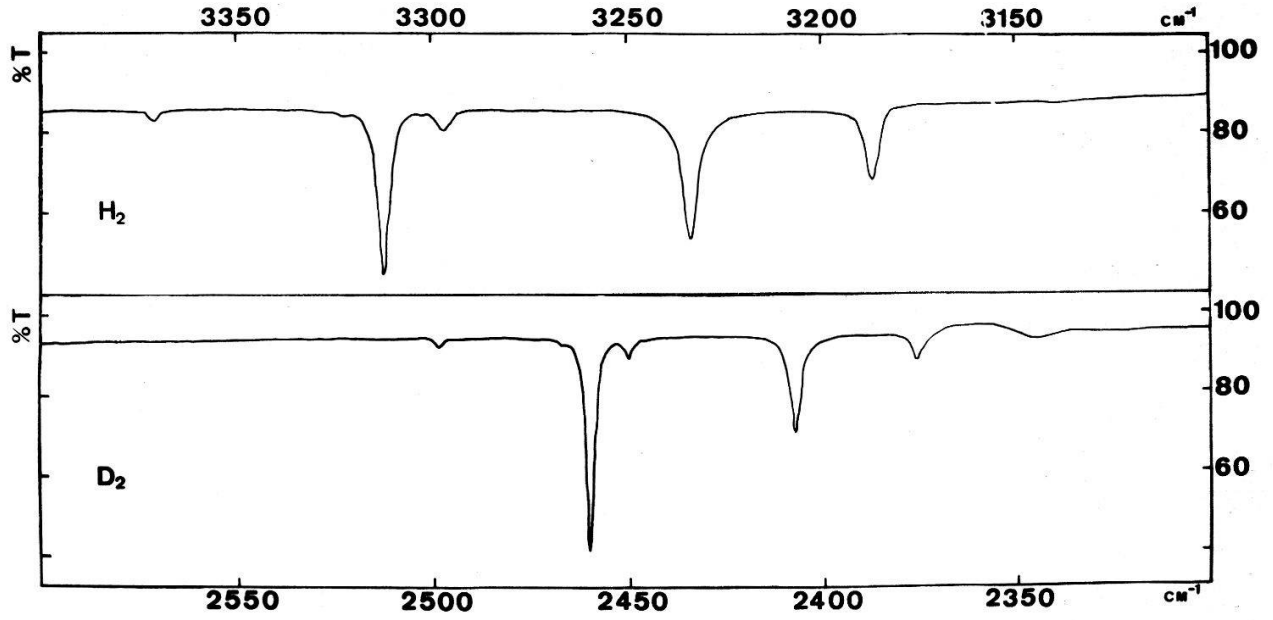

Figure 12
LN_2 Temperature near IR Spectra of the reduced State of α-Al_2O_3: (Fe, Ti) after Reduction by H_2 and by D_2.

Table 4
Isotope Effect of Reduction by D_2 instead of H_2 on the near IR Spectrum of α-Al_2O_3: (Fe, Ti).

$\tilde{\nu}_{OH}$	$\tilde{\nu}_{OD}$	$\tilde{\nu}_{OH}/\tilde{\nu}_{OD}$
3371.0 cm^{-1}	2501.1 cm^{-1}	1.3478
3312.5	2464.0	1.3443
3296.8	2452.0	1.3445
3234.0	2410.0	1.3419
3187.4	2380.0	1.3392
	average value	1.3435
theoretical ratio for $\tilde{\nu}_{OH}/\tilde{\nu}_{OD}$ ($C_{\infty v}$)		1.374
theoretical ratio for $\tilde{\nu}_{OHO}/\tilde{\nu}_{OD}$ ($D_{\infty h}$)		1.393

ESR Results of Reduced und Oxidized States

The ESR results reported here are intended to give information about the valence states of the transition metal ions and their changes upon redox treatment. In the case of Fe and (Fe, Ti) doped crystals it was furthermore possible to measure the changes in concentration of Fe^{+3} produced by redox treatment. In this group of experiments the latter consisted of exposure of the crystals to H_2 or O_2 atmosphere at 1550–1600 °C for 60 hours.

1. Fe^{+3} *in* α-Al_2O_3:Fe *and* α-Al_2O_3:(Fe, Ti) *systems*

Using the procedure described in Section 2 the results collected in Table 5 were obtained, which should be completed by the following statements:

(i) Line shape analysis reveals that for Fe doped crystals better fits were obtained by Gaussian shapes whereas for α-Al_2O_3:(Fe, Ti) Lorentzian shapes are more appropriate.

(ii) The line width of the Fe^{+3} signal obtained with peripheral α-Al_2O_3:(Fe, Ti) samples reveals a distinct difference between the reduced and oxidized states, amounting to approximately 21 and 24.5 Gauss respectively. For samples cut from the central part and from α-Al_2O_3:Fe no significant line width alteration was observed.

(iii) It was generally found, that the line width depends on the ion concentration, i.e. is markedly larger in the peripheral zone of α-Al_2O_3:(Fe, Ti).

Using the results reported in Section 3 about electron microprobe analysis one may draw conclusions concerning the absolute concentration of Fe^{+3} in the different states.

Table 5
Relative Fe^{+3}-Concentration in Reduced and Oxidized State.

State	α-Al_2O_3: (Fe, Ti)		α-Al_2O_3: Fe
	center	periphery	
raw	1.805 ± 0.028	4.387 ± 0.077	1.007 ± 0.025
oxidized	2.084 ± 0.022	5.404 ± 0.068	1.149 ± 0.027
reduced	1.423 ± 0.029	3.736 ± 0.073	0.548 ± 0.007
oxidized	2.770 ± 0.058	5.561 ± 0.064	1.163 ± 0.026

2. Ti^{+3} *in* α-Al_2O_3:Ti *and* α-Al_2O_3:(Fe, Ti) *crystals*

The ESR signal of α-Al_2O_3:Ti^{+3} has been investigated by Kornienko and Prokhorov [10] who reported a single line signal with approximately 50 G line width below 9 K. Above this temperature the line width increased. No quantitative measurements of line strength was possible in this work owing to technical difficulties at LHe temperature. These also excluded comparison between measurements on different samples leading to only qualitative estimates of signal strength.

The results collected in Table 6 have been obtained from measurement of Ti and (Fe, Ti) doped samples in the raw and the oxidized state. The following remarks should be made:

(i) No sample (in either state) gave detectable splittings or significant line width changes.

(ii) For α-Al_2O_3:Ti the decrease of the Ti^{+3} signal upon oxidation of the raw state is significant.

(iii) In the case of α-Al_2O_3:(Fe, Ti) samples oxidation of the raw state may also have involved a decrease of the Ti^{+3} signal, but there is doubt owing to resettability problems with the LHe measurement.

Table 6
Approximate Relative ESR Signal Intensity of Ti^{+3} a).

State	α-Al_2O_3: (Fe, Ti)	α-Al_2O_3: Ti
raw	100	1
oxidized	1	1/16

a) Measurement with magnetic field parallel to crystallographic c axes.

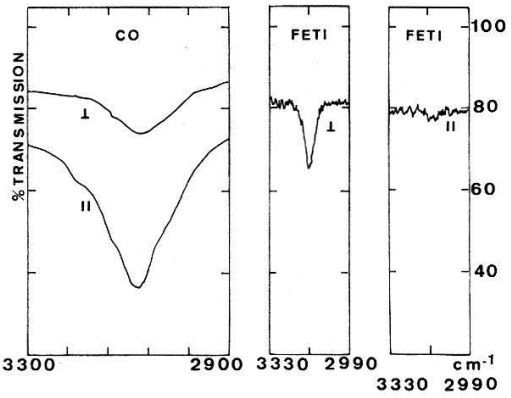

Figure 13
Polarized near IR Spectra of the Reduced State of α-Al_2O_3:Co and α-Al_2O_3:(Fe, Ti).

4. Discussion

In order to rationalize the solid state reactions studied in this work discussion will be made in sections. First infrared spectra will be considered because of their bearing to the structure of the transition metal ion and its near surroundings. Then the valence states of the former will be correlated to the optical and ESR spectra and finally a reaction scheme including approximate thermodynamic aspects is suggested.

Conclusion from Infrared Spectra

From comparison with results published in paper I and by Hauffe et al. [9] considerable differences in the structure of the 3 μ IR bands are found between Ni- and Co-doped α-Al_2O_3 on one hand and Fe, Ti and (Fe, Ti) substituted sapphire on the other hand. All essential features of the near IR spectra are collected in Table 7 comprising frequency, half width $\tilde{\nu}_{1/2}$, polarization and frequency shift $\Delta\tilde{\nu}_s = \tilde{\nu}(OH)_{free} - \tilde{\nu}(OH)$. Whereas the first group exhibits broad bands extending from 3300 to 2900 cm^{-1} accompanied by a group of sharp weak bands near 2300 cm^{-1}, the second

group shows only one group of sharp bands near 3400–3100 cm^{-1}. In both cases however the bands may be assigned unambigously to OH stretching vibrations by their deuterium isotope shift (cf. Section 3).

Table 7
Data of Near IR Absorption Bands of Various Substituted Sapphire.

Experimental Data				Calculated Data[a]			
ν_s	$\Delta\tilde{\nu}_s$	$\tilde{\nu}_{1/2}$	Pol[c] $\parallel : \perp$	$\tilde{\nu}_{1/2}$ from $\Delta\tilde{\nu}_s$	0...0 distance from $\tilde{\nu}_s$	0...0 distance from $\Delta\tilde{\nu}_s$	occurrence
3025 cm^{-1}	625 cm^{-1}	130 cm^{-1}	5:1	470 cm^{-1}	2.74 Å	2.70 Å	α-Al_2O_3: Co
2972	678	180	5:1	520	2.72	2.69	α-Al_2O_3: Ni
3180	470	4 [b]	n.m.	232	2.76	2.73	α-Al_2O_3: Fe
3230	420	6	n.m.	318	2.78	2.75	α-Al_2O_3: Fe α-Al_2O_3: Ti
3310	340	3 [b]	0	230	2.84	2.78	α-Al_2O_3: (Fe, Ti)

[a] c.f. Ref. [29].
[b] Spectra measured at 77 K.
[c] $\parallel : \perp$ means intensity ratio measured for $\parallel$ and $\perp$ polarized radiation with respect to the crystallographic c-axis.

From Table 4 considerable deviations between observed and predicted isotope shifts are to be noted. The latter are calculated by the harmonic approximation, but should be corrected for anharmonicity effects. If the approximate relation $\nu = \omega_e(1 - 2x_e)$ between fundamental and normal frequency [27], and the relation $x_e/x'_e = \omega_e/\omega'_e$ proposed by Dennison [28] are used, one obtains $2x_e = 8.02 \cdot 10^{-2}$ and $2x_e = 12.47 \cdot 10^{-2}$. The latter value indeed is unusually high and leads to the conclusion that the infrared absorption probably has to be ascribed to a O–H type rather than to a OHO symmetrical type vibrator.

Using empirical relations between isotope shift $\Delta\tilde{\nu}_s$ and 0 . . . 0 distance proposed by several authors [29] it has been inferred for the Ni- and Co-sapphire, that the proton is situated between oxygen ion pairs O_2 . . . O_3, cf. Figure 14. As an immediate consequence partial polarization parallel to c would be expected. This is born out by a polarization ratio $I_\perp/I_\parallel = 1/5$ found experimentally (cf. Fig. 13). Furthermore the large half width of the ν(OH) bands of Ni- and Co-sapphire supports the view of an intermolecular hydrogen bond, supposing the O^{-2} triangle in adjacent layers to be considered as different 'molecules'.

Using the same type of argument for hydrogen bonding for the Fe-, Ti- and (Fe, Ti)-substituted sapphire, the IR spectra of these crystals in the reduced state indicate an 0 . . . 0 distance of 2.73–2.78 Å, which is significantly larger than in the Ni- and Co-dopped sapphire. This may be identified with the 2.87 Å distance of $O_1 \ldots O_2$ pairs, cf. Figure 14. Accordingly the ν(OH) band should be polarized perpendicular to c, which is experimentally confirmed (cf. Fig. 13). Furthermore, the small halfwidth $\tilde{\nu}_{1/2}$ points to an intramolecular hydrogen bond, supporting the view of considering the O^{-2} triangles (O_1 . . . O_2 . . . O_5) as 'molecules'.

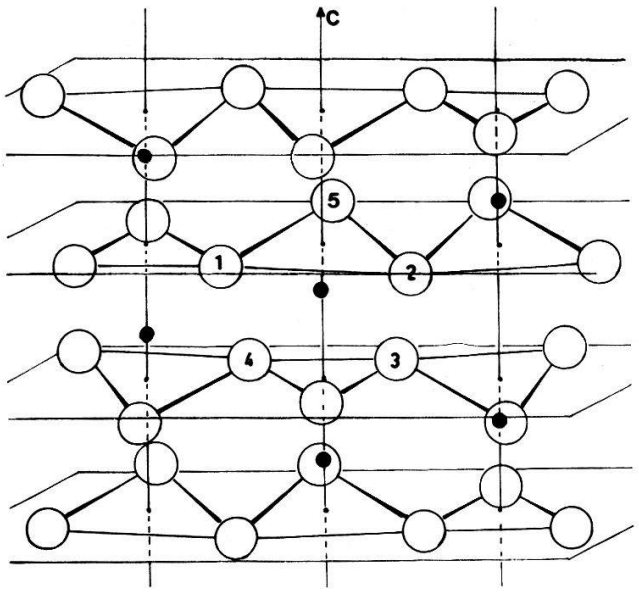

Figure 14
Structure of α-Al_2O_3 (reprinted from Ref. [8]).

No attempt has been made in the frame of this work to extract more information about the structure of the defects produced by the transition metal ion in the reduced state substituted in sapphire. Also the nature of the 2300 cm^{-1} bands of Ni- and Co-sapphire has not been elucidated so far.

Valence State of Transition Metal Ions

In this section first the results of extensive crystal field calculations for α-Al_2O_3: Fe^{+3} and α-Al_2O_3: Ti^{+3} are given and the problems arising in their use for interpretation of empirical spectra will be pointed out. Also comparison of the assignments for Fe^{+3} crystal field bands presented by other authors is made. Furthermore behaviour and interrelation of the 385 nm and 450 nm band groups of Fe- and (Fe, Ti)-sapphire with the Fe^{+3} ESR results is reviewed, leading to the assignment of this group to the crystal field spectrum of α-Al_2O_3: Fe^{+3}. Finally a discussion of the valence states of Ti in both α-Al_2O_3: Ti and α-Al_2O_3: (Fe, Ti) is added.

1. *Crystal Field Treatment for* α-Al_2O_3: Fe^{+3}

As will be shown in the next section the 385 and 450 nm bands in α-Al_2O_3: (Fe, Ti) must be correlated to the α-Al_2O_3: Fe^{+3} crystal field.

In order to obtain a guiding line for the assignment of these absorptions extensive crystal field calculations were carried out. These were made within the same frame as used earlier for calculation of defect spectra in ruby [14]. For details the reader is referred to this paper and only points relevant to the work reported here are mentioned.

(i) For the ions Fe^{+3} and Ti^{+3} all 3 d^n electron configurations and all Russell-Saunders states resulting from these were included in the calculation. Spin orbitals were constructed from numerically given SCF Hartree Fock orbitals [30] from which also the radial integrals $\langle r^k \rangle$ were calculated by numerical integration:

$$Ti^{+3}: \langle r^2 \rangle = 0.53405 \text{ Å}^2, \quad \langle r^4 \rangle = 0.57689 \text{ Å}^4, \tag{3}$$

$$Fe^{+3} \langle r^2 \rangle = 0.31958 \text{ Å}^2, \quad \langle r^4 \rangle = 0.22362 \text{ Å}^4. \tag{4}$$

(ii) Since in the $|\, J\, J_3\rangle$ base the LS coupling operator is diagonal, its matrix elements for the free ion [31] could be used directly. The relevant site group for both transition metal ions in site c [35] is the double group C_3^*, hence the $|\, J\, J_3\rangle$ basis functions belong directly to the irreducible representations Γ_{J3} of C_3^*. For 3 d^5 and 3 d^1 systems in particular only the integer representations $\Gamma_{1/2}$, $\Gamma_{3/2}$, $\Gamma_{5/2}$ occur and as a consequence the energy matrix factorizes into 3 blocks which were diagonalized numerically.

For inclusion of the Zeeman Effect the matrix of the Zeeman Operator

$$\hat{H}_z = \mu_e(H_0, \hat{L} + |\, g_e\,|\, \hat{S}) \tag{5}$$

was calculated in the $|\, J\, J_3\rangle$ basis by the formulae given by Slater [32] and added to the crystal field matrix before diagonalization.

(iii) As has been found by several authors, $\langle r^4\rangle$ values derived from SCF Hartree-Fock orbitals of the free ion may lead to considerable discrepancies between optical transitions calculated by crystal field theory and observed spectra [33]. In the frame of Slater type atomic orbitals $R_n \propto r^{n-1} \cdot e^{-\alpha r}$ and therefore

$$\frac{\langle r^2\rangle}{\langle r^4\rangle} = (2\,\alpha)^2 \frac{\Gamma(2\,n+3)}{\Gamma(2\,n+5)}\,. \tag{6}$$

On the other hand for a trigonally distorted cubic crystal field splitting of 3 d orbitals depends linearly on $\langle r^4\rangle$ and $\langle r^2\rangle$. In this work $\langle r^4\rangle$ will therefore be considered as an empirical parameter, keeping $\langle r^2\rangle$ coupled to $\langle r^4\rangle$ by relation (6). Indeed $\langle r^4\rangle$ depends critically on the information available for the SCF orbitals and may be influenced most strongly by covalent interactions between the ion substituted and the O^{-2} ions of the lattice.

Results of the crystal field computations are presented in Figure 15 which gives the crystal field levels of the Fe^{+3} at site c as a function of $\langle r^4\rangle$ [34]. In the r.h.s. the observed transitions of α-Al_2O_3:Fe^{+3} near 385 and 450 nm are marked. They may be commented upon as follows:

(i) The crystal field level pattern was calculated for the $\langle r^4\rangle$ value of the free ion ($\langle r^4\rangle = 0.22$ Å) and two other points at arbitrally chosen values $\langle r^4\rangle = 0.68$ Å^4 and 2.2 Å^4. The lines connecting corresponding levels in the calculated patterns represent linear interpolation.

(ii) Since it is obvious from Figure 15 that the level pattern for the free ion case (*a*) deviates grossly from the observed band group near 385 nm, use of a $\langle r^4\rangle$ value different from that of the free ion is proposed. Possible assignment were obtained for $\langle r^4\rangle$ values 0.6, 1.0 and 1.8 Å^4 (points *b*, *c* and *d*, respectively marked in Fig. 15) and are represented graphically in more detail in the upper part of Figure 15 in relation to the empirical spectrum. It showns that none of these gives perfect agreement. Very close agreement may barely be expected, since the crystal field model used here still contains some serious simplifications, e.g. neglect of covalence, higher multipole terms in the crystal field expansion and extended electron configurations like 3 d^4 4 s or 3 p^5 3 d^6, linear interpolation, etc. From empirical polarizations discrimination between these 3 possible assignments cannot be given. This follows from the behaviour of the ^{6}S ground state, which in the group C_3^* goes over into $2\,\Gamma_{1/2} + 2\,\Gamma_{3/2} + 2\,\Gamma_{5/2}$, whose energies are equal in the C_3^* crystal field. As a consequence transitions with

both || and | polarization are allowed. Since no Zeeman effect has been detectable, no discrimination among the C_3^* substates is possible. As may be seen from Figure 15 one is tempted to chose the levels for $\langle r^4 \rangle = 1.0$ Å^4 as a best compromise if the 450 nm band observed with α-Al_2O_3-Fe^{+3} (cf. section 3 and Fig. 6, 8) is included. The relation of this assignment (cf. Table 3) to assignments presented by other workers will be discussed briefly below.

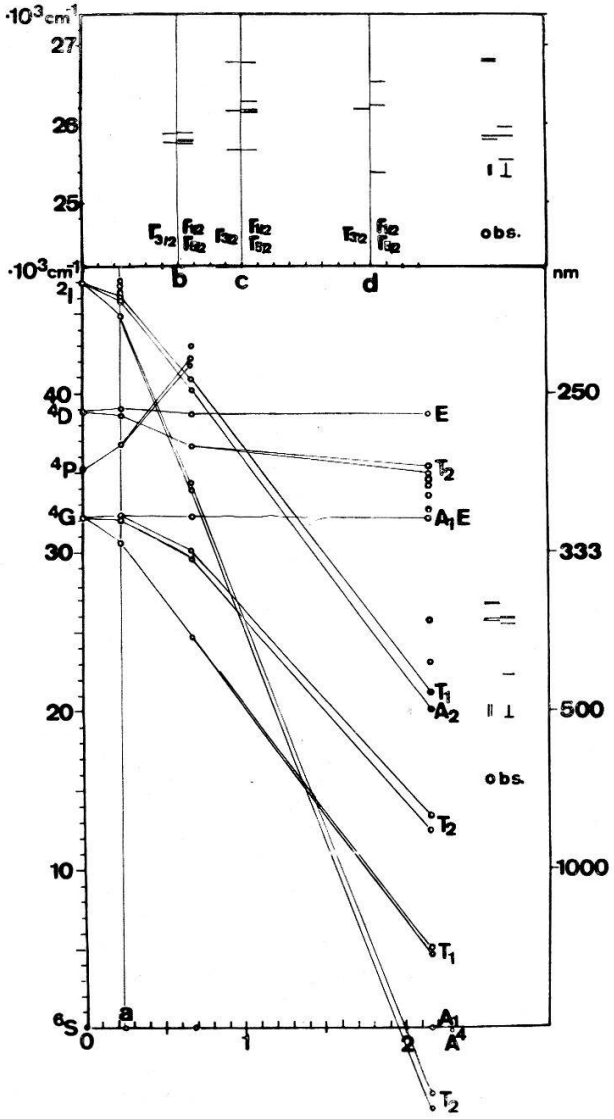

Figure 15
$\langle r^4 \rangle$ Dependence of Crystal Field Levels of α-Al_2O_3: Fe^{+3} (at the l.h.s. free ion terms are given, at the r.h.s. crystal field notations (0) and observed line positions are marked. In the upper part details of the 385 and 450 nm region are given.

A view of the general correctness of the crystal field procedure used in this work is born out by results obtained on Ti^{+3} substituted in α-Al_2O_3. These are reproduced in Figure 16 from which a value of $\langle r^4 \rangle = 1.3$ Å^4 was derived in order to get a satisfactory agreement between observed and calculated *d-d* transition frequency. Comparison shows that this is again considerably larger than the SCF Hartree-Fock value for the free ion.

2. *Comparison with other Assignments*

McClure [1] observed with α-Al_2O_3:Fe a band near 549 nm (18200 cm^{-1}) which was assigned to the crystal field transition $^6A_1 \rightarrow {}^4T_2$. This band could be observed neither in this work nor by Lehmann et al. [11]. From our measurement on 100 ppm

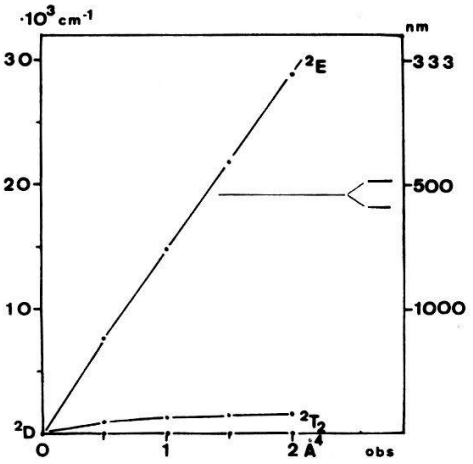

Figure 16
$\langle r^4 \rangle$ Dependence of Crystal Field Levels of α-Al_2O_3: Ti^{+3} in site *c* (at the l.h.s. free ion terms are given, at the r.h.s. crystal field notations (0) and observed line positions are marked).

Fe containing crystals up to 8 mm thickness one may conclude that max. $\varepsilon(549) < 3.6$ l/mol/cm. The band group near 385 nm (25600 cm^{-1}) has been found with much higher doped crystals but has only been partly resolved by McClure and Lehmann et al. Besides this and a systematic shift however their results are confirmed by the highly resolved spectra given in Figure 8. McClure assigned these bands to the transition $^6A_1 \rightarrow {}^4A_1 + {}^4E$, whereas Lehmann et al. interpret the bands at 376, 389 and 452 nm as $^6A_1 \rightarrow {}^4E(D)$, $^6A_1 \rightarrow {}^4T_2(D)$ and $^6A_1 \rightarrow {}^4A_1(G) + {}^4E(G)$ respectively. Finally the bands found by Lehmann et al. near 568 and 697 nm with much higher doped α-Al_2O_3:Fe crystals (1200 ppm) could not be detected in crystals containing only Fe in this work. According to the present crystal field calculations both these assignments for the 385 and 450 nm bands concern upper levels which are nearly unaffected by the Al_2O_3 crystal field (cf. Fig. 15) and would be expected at considerably higher frequencies (30000 . . . 40000 cm^{-1}). Since the bands near 568 and 697 nm were found to be not related to Fe^{+3}, but to (Fe, Ti), it is felt that the assignment presented in this work in Table 3 gives a more appropriate interpretation of the Fe^{+3} spectrum. The latter two bands should rather be ascribed to the pair particle α-Al_2O_3:(Fe, Ti)$^{+6}$, according to our analytical and spectroscopic data. Further discussion devoted to this interpretation is presented below. On the other hand the bands near 810 and 640 nm found by Lehmann et al. [11] with highly doped natural sapphire which these authors assigned to Fe^{+2} were never observed in this work with reduced α-Al_2O_3:Fe or α-Al_2O_3:(Fe, Ti). From this fact we conclude that these bands are not relevant for the blue colour of α-Al_2O_3:(Fe, Ti)$^{+6}$.

3. *Valence states of* Fe *in* α-Al_2O_3:Fe *and* α-Al_2O_3:(Fe, Ti)

From the experimental results of optical, Zeeman and ESR studies presented in Section 3, the 385 nm band group and the 450 nm band may unambigously be assigned to Fe^{+3} crystal field transitions. The argument are as follows:

(i) The 385 nm bands have been observed to our knowlegde only with Fe containing sapphire.

(ii) The intensity variation of these bands produced by reduction and oxidation parallels the intensity variation of the Fe^{+3} ESR signal (cf. Table 5).

(iii) The results of the high resolution optical and Zeeman measurements do not conflict with this assignment, though they do not definitely prove it.

4. *Valence states of* Ti *in* α-Al_2O_3:Ti *and* α-Al_2O_3:(Fe, Ti)

For the system α-Al_2O_3:Ti it may be concluded from Table 6 and optical spectra Figure 7, that in the reduced state Ti^{+3} is present. As a conclusion from the absence of Ti^{+3} optical and ESR signals in the oxidized state one may assume Ti^{+3} to be dominant.

The system α-Al_2O_3:(Fe, Ti) is more complex (cf. Table 6).

(i) In neither the oxidized nor the reduced state was the optical spectrum of Ti^{+3} detectable.

(ii) The ESR-signal of Ti^{+3} in both the oxidized and the reduced state was very weak.

(iii) Information about an upper limit of the concentration of Ti^{+3} in α-Al_2O_3:(Fe, Ti) may be obtained by means of the optical spectra. From Figure 7, which relates to the Ti^{+3} spectrum, and Figure 4 one obtains for the extinction coefficient at 490 nm $\varepsilon = 22.2\,\mathrm{l\,mol^{-1}\,cm^{-1}}$, assuming that all Ti was present in the reduced state as Ti^{+3}. Using a reproducibility of 4% for transmission measurements this leads to a detectability limit of 12 ppm Ti^{+3}.

Therefore from (i)–(iii) one may conclude, that the Ti^{+3} concentration in both the reduced and the oxidized state of α-Al_2O_3:(Fe, Ti) never exceeded 12 ppm.

Solid State Reactions

From the results and discussion presented so far, one may now propose a system of solid state redox reactions. Since at the present time no experimental thermochemical data for these thermochemical processes are available, $\Delta H^0(0) \approx \Delta U^0(0)$ values were calculated within a Haber-Born type framework (the following notation is used: Fe^{+3} (c, α-Al_2O_3) means Fe^{+3} in site c (Wykoff-Notation [35]) of α-Al_2O_3):

$$M^{+z}(c, Al_2O_3) \rightarrow M^{+z}(g)\,, \tag{7}$$

$$M^{+z}(g) + e^- \rightarrow M^{+(z-1)}(g)\,, \tag{8}$$

$$M^{+(z-1)}(g) \rightarrow M^{+(z-1)}(c, Al_2O_3)\,, \tag{9}$$

$$\frac{1}{2}\,H_2(g) \rightarrow H(g)\,, \tag{10}$$

$$H(g) \rightarrow H^+(g) + e^-\,, \tag{11}$$

$$H^+(g) \rightarrow H^+(Al_2O_3)\,, \tag{12}$$

$$H_2(g) + \frac{1}{2}\,O_2(g) \rightarrow H_2O(g)\,. \tag{13}$$

For transition metal ions the atomic energy levels [31] and lattice potentials calculated by P. Ballmer et al. [36] were used to calculate the $\Delta H^0(0)$'s of reactions (7), (8) and (9). The data for reaction (10), (11) and (13) have been taken from a NBS Publication [37]. Table 8 gives the $\Delta H^0(0)$ values for relevant reactions.

No reliable thermodynamic data may be derived for the model proposed in the preceeding sections for $H^+(Al_2O_3)$ on spectroscopic arguments. Though the proton is situated between O^{-2} ions in sites e and therefore its crystal field energy may be

calculated from the electrostatic crystal field potential [14], bonding in the particle $O \ldots H \ldots O^{-3}$ may be expected to involve considerable covalent contributions. Since from IR spectra it may be concluded that the particle has the same structure for all 3 systems studied in this work, reaction (12) may be defined as a reference reaction with well defined but unknown $\Delta H^0_{12}(0)$. A crystal field estimate of $\Delta H^0_{12}(0)$ has been calculated in an earlier paper.

As mentioned above, two of the systems studied in this work showed a certain irreversibility in the first step of thermal treatment. The solid state reactions responsible for this phenomenon will now be discussed for each particular systems.

1. α-Al_2O_3:Fe^{+3}/Fe^{+2}

As pointed out in section 3 H_2 treatment of raw α-Al_2O_3:Fe yielded no $\tilde{\nu}$(OH) bands, these appeared only after O_2 treatment preceeding the H_2 treatment. Both H_2 and O_2 treatment and further heat treatment eliminated the near UV band at 395 nm. From ESR measurements one may conclude, that Fe^{+3} concentration was nearly equal in raw and oxidized states.

Unfortunately the information available at present time does not enable us to give a substantiable interpretation of this behaviour, in particular of the surprising fact, that H_2 treatment of raw crystals produced no $\tilde{\nu}$(OH) bands. A similar behaviour has been found with defect rubies [14]. However in that case the first thermal treatment was shown to involve extraction of Na^+ and K^+ by diffusion into the gas phase. On the other hand the 395 nm band of raw state seems to be attributable to a thermal defect, which could not be regenerated by UV irradiation.

From the experimental data one may show the following steps to be responsible for the redox behavior:

$$Fe^{+3}(c, Al_2O_3) + \frac{1}{2} H_2(g) \rightarrow Fe^{+2}(c, Al_2O_3) + H^+(Al_2O_3)\,, \tag{14}$$

$$Fe^{+2}(c, Al_2O_3) + H^+(Al_2O_3) + \frac{1}{4} O_2(g) \rightarrow Fe^{+3}(c, Al_2O_3) + \frac{1}{2} H_2O(g)\,. \tag{15}$$

From Table 8 one obtains $\Delta H^0_{14}(0) = +\,537$ kcal/mol and $\Delta H^0_{15}(0) = -\,563$ kcal/mol expressing the reversibility of the redox process. However it remains to explain the fact, that by H_2 treatment never more than approximately half the Fe^{+3} could be

Table 8
$\Delta H^0(0)$ Values of Reaction Steps Relevant for Redox Processes.

Reaction		$\Delta H^0(0)$ in kcal/mol $M^{+z} = Fe^{+3}$	$M^{+z} = Ti^{+4}$
$M^{+z}(c, Al_2O_3)$	$\rightarrow M^{+z}(g)$	+ 2466	+ 3288
$M^{+z}(g) + e^-$	$\rightarrow M^{+(z-1)}(g)$	− 703	− 988
$M^{+(z-1)}(g)$	$\rightarrow M^{+(z-1)}(c, Al_2O_3)$	− 1644	− 2466
$1/2\ H_2(g)$	$\rightarrow H(g)$	+ 51.6	
$H(g)$	$\rightarrow H^+(g) + e^-$	+ 314.2	
$H^+(g)$	$\rightarrow H^+(Al_2O_3)$	+ 52.0[a])	
$H_2(g) + 1/2\ O_2(g)$	$\rightarrow H_20(g)$	− 57.1	

[a]) Upper limit, c.f. Ref. [14].

reduced, cf. Table 5. The only interpretation available at present seems to be the increase of ionic radii on reduction, which are 0.76 and 0.64 Å for Fe^{+2} and Fe^{+3} respectively. Apparently a considerable relaxation of the α-Al_2O_3 structure is produced with increase of the reduction reaction, leading to a more positive $\Delta H^0_{14}(0)$. This interpretation is supported by the fact, that the transparency of α-Al_2O_3:Fe decreased noticeably with the reduction process.

2. α-Al_2O_3:Ti^{+3}/Ti^{+4}

The experimental data presented in Section 3 gives strong evidence that the valence states of Ti in α-Al_2O_3:Ti involved in redox reactions should be identified with Ti^{+3} and Ti^{+4}. With respect to charge compensation, Ti therefore takes a unique position among the systems studied so far in our laboratory, which obviously has to be traced back to thermodynamic stability of Ti^{+4}. The following model appears to be compatible with experimental information:

$$\text{raw state:} \quad Ti^{+3}(c, Al_2O_3) + \frac{1}{3}[Na^{+}(c, Al_2O_3) + VO^{-2}(e, Al_2O_3)] , \tag{16}$$

$$\text{oxidized state:} \quad Ti^{+4}(c, Al_2O_3) + \frac{1}{3} VAl^{+3}(c, Al_2O_3) , \tag{16'}$$

$$\text{oxireduced state:} \quad Ti^{+3}(c, Al_2O_3) + \frac{1}{3} VAl^{+3}(c, Al_2O_3) + H^{+}(Al_2O_3) . \tag{16''}$$

Here $VO^{-2}(c, Al_2O_3)$ and $VAl^{+3}(e, Al_2O_3)$ denote an Al^{+3} vacancy in site c and an O^{-2} vacancy in site e, respectively. This model requires a relatively small concentration of vacancies and ot the impurity ions Na^+ or K^+ (1/3 of Ti concentration).

Oxidation of the raw state (16) produces by thermal extraction of Na or K according to reaction (17):

$$3\,Ti^{+3}(c, Al_2O_3) + Na^{+}(c, Al_2O_3) + O_2(g) + VO^{-2}(e, Al_2O_3) \rightarrow 3\,Ti^{+4}(c, Al_2O_3) + VAl^{+3}(c, Al_2O_3) + O^{-2}(e, Al_2O_3) + \frac{1}{2} Na_2O_2(s) . \tag{17}$$

For the system α-Al_2O_3:Ti alkali metal extraction has not directly been measured by analytical methods. However in the case of defect ruby, this process has been proven to take place during the first high temperature treatment [14]. We therefore believe this process to be relevant also for the irreversible behaviour of α-Al_2O_3:Ti in the first step of thermal treatment. The feasiblity of reaction (17) may be substantiated by thermodynamic considerations. In Table 9 the $\Delta H^0(0)$'s of all elementary steps are collected from which $\Delta H^0_{17}(0)$ may be estimated by the same type of arguments as used for Table 8. It should be pointed out, that the scheme (16) does not represent the only possibility to explain the behaviour of α-Al_2O_3:Ti. Charge compensation for substitution of Ti^{+4} in the α-Al_2O_3 lattice structure could be provided by substitution of N^{-3} for O^{-2}. However under the conditions of the Verneuil method applied for growth of the samples used in this work, substitution of N^{-3} appears highly unprobable. Alternatively substitution of pairs (Ti^{+4}, Me^{+2}) would be compatible with

electroneutrality. However analytically Me^{+2} (transition metal or earth alkali ions) have not been found in concentration sufficient for charge compensation of the $Ti^{+4} \leftrightarrow Ti^{+3}$ process.

Table 9
Thermodynamic Data of Redox Reactions of α-Al_2O_3: Ti System.

Reaction		$\Delta H^0(0)$ in kcal/mol
$3\ Ti^{+3}(c, Al_2O_3)$	$\rightarrow 3\ Ti^{+3}(g)$	+ 2466
$3\ Ti^{+3}(g) - 3\ e^-$	$\rightarrow 3\ Ti^{+4}(g)$	+ 988
$3\ Ti^{+4}(g)$	$\rightarrow 3\ Ti^{+4}(c, Al_2O_3)$	− 3288
$Na^+(c, Al_2O_3)$	$\rightarrow Na^+(g)$	+ 822
$Na^+(g) + e^-$	$\rightarrow Na(g)$	− 110
$Na(g)$	$\rightarrow Na(s)$	− 26
$Na(s) + 1/2\ O_2(g)$	$\rightarrow 1/2\ Na_2O_2(s)$	− 61
$1/2\ O_2(g)$	$\rightarrow O(g)$	+ 58
$O(g) + 2\ e^-$	$\rightarrow O^{-2}(g)$	+ 170
$O^{-2}(g)$	$\rightarrow O^{-2}(e, Al_2O_3)$	− 1260
Oxidation of raw state	$\Delta H^0(0)$	− 241

For the reversible redox process

$$Ti^{+4}(c, Al_2O_3) + \frac{1}{2} H_2(g) \rightarrow Ti^{+3}(c, Al_2O_3) + H^+(Al_2O_3)\,, \qquad (18')$$

$$Ti^{+3}(c, Al_2O_3) + H^+(Al_2O_3) + \frac{1}{4} O_2(g) \rightarrow Ti^{+4}(c, Al_2O_3) + \frac{1}{2} H_2O(g)\,. \qquad (18'')$$

$\Delta H^0_{18'}(0) \simeq +\ 252$ kcal/mol and $\Delta H^0_{18''}(0) \simeq -\ 279$ kcal/mol is obtained from Table 8. In equation (18′) and (18″) the charge compensating Al^{+3} vacancy (cf. (16)) is not involved and thus not given explicitly.

3. α-Al_2O_3:(Fe, Ti)

For this system practically no irreversible steps have been found. From the results presented in Section 3, the following facts should be rementioned:

(i) In the oxidized state all Fe was found in the form of Fe^{+3}.

(ii) By H_2 treatment part of the Fe^{+3} disappeared. Very probably this part was present in the reduced state as Fe^{+2}.

(iii) In both the oxidized and the reduced state most of the Ti must have been present as Ti^{+4} as has been discussed in the section above.

(iv) The VIS spectrum of α-Al_2O_3:(Fe, Ti) is very different from those of the single doped varieties. The bands at 565 and 700 nm (cf. Fig. 8) clearly indicate, that it has to be assigned to a new particle and cannot be derived from the spectra of the single particles Ti and Fe. This is born out also by the analytical data shown in Figure 4 and Figure 8.

The following interpretation may be given: Several workers [38] suggested the existence of biparticles from magnetic and optical measurements, however to our knowledge no direct analytical proof of biparticle formation has been given so far.

For the system α-Al_2O_3:(Fe, Ti) one would have to assume the system of solid state reactions to express biparticle formation:

$$\mathrm{Fe}(c) + \mathrm{Fe}(c) \rightarrow (\mathrm{Fe}, \mathrm{Fe})\ (c, c)\ , \tag{19'}$$

$$\mathrm{Ti}(c) + \mathrm{Ti}(c) \rightarrow (\mathrm{Ti}, \mathrm{Ti})\ (c, c)\ , \tag{19''}$$

$$\mathrm{Ti}(c) + \mathrm{Fe}(c) \rightarrow (\mathrm{Fe}, \mathrm{Ti})\ (c\ ,c)\ . \tag{19'''}$$

In the left hand sides of these equations the dopants were assumed to be substituted in site c situated at large distance from each other, whereas in the r.h.s. pairs of ions were substituted in adjacent c sites. Reactions (19) may be considered to symbolize biparticle formation during the flame fusion process. As the crystal was cooled below the melting point, mobility of the ions droped and the biparticles were frozen at a concentration corresponding to a near melting point temperature equilibrium. For the system (19) application of Lambert Beers law yields

$$D(\lambda, r) = L\{\varepsilon_{\mathrm{Fe}}[\mathrm{Fe}] + \varepsilon_{\mathrm{Fe_2}}[\mathrm{Fe_2}] + \varepsilon_{\mathrm{Ti}}[\mathrm{Ti}] + \varepsilon_{\mathrm{Ti_2}}[\mathrm{Ti_2}] + \varepsilon_{\mathrm{FeTi}}[\mathrm{Fe\ Ti}]\}\ , \tag{20}$$

where D, L and the ε's denote optical density, layer thickness and the extinction coefficients of the defects at a given wavelength λ and a given radial position r. Then using the chemical equilibrium equations of the reactions (19):

$$K_{\mathrm{Fe_2}} = \frac{[\mathrm{Fe_2}]}{[\mathrm{Fe}]^2}\ , \tag{21'}$$

$$K_{\mathrm{Ti_2}} = \frac{[\mathrm{Ti_2}]}{[\mathrm{Ti}]^2}\ , \tag{21''}$$

$$K_{\mathrm{FeTi}} = \frac{[\mathrm{Fe, Ti}]}{[\mathrm{Fe}]\,[\mathrm{Ti}]}\ . \tag{21'''}$$

Equation (20) became, after solution for the total concentrations $[\mathrm{Fe}]_0$ and $[\mathrm{Ti}]_0$:

$$\begin{aligned} D(\lambda, r) = {} & D_0(\lambda, r) + \varepsilon_{\mathrm{Fe}}[\mathrm{Fe}]_0 + \varepsilon_{\mathrm{Ti}}[\mathrm{Ti}]_0 \\ & + [-2\,\varepsilon_{\mathrm{Fe}} + \varepsilon_{\mathrm{Fe_2}}]\,K_{\mathrm{Fe_2}}[\mathrm{Fe}]_0 \\ & + [-\varepsilon_{\mathrm{Fe}} - \varepsilon_{\mathrm{Ti}} + \varepsilon_{\mathrm{FeTi}}]\,K_{\mathrm{FeTi}}[\mathrm{Fe}]_0 \cdot [\mathrm{Ti}]_0 \\ & + [-2\,\varepsilon_{\mathrm{Ti}} + \varepsilon_{\mathrm{Ti_2}}]\,K_{\mathrm{Ti_2}}[\mathrm{Ti}]_0^2 + \cdots . \end{aligned} \tag{22}$$

The data presented in Figure 5 and Figure 10 could now be analysed according to (22) by multiple regression in order to prove the significance of terms of 2nd order. We obtained the results in Table 10, which should be commented upon as follows [26]:

(i) Quadratic and bilinear terms are significant, indicating significant biparticle formation.

(ii) On statistical arguments it cannot be significantly distinguished from the different types of biparticle formation processes expressed by (19).

For none of the statistically acceptable models No. 2, 3, 4 could all the physical parameters (ε's and K's) be derived from the regression coefficients. This is seen from equation (22), which shows the number of physical parameters being larger than that of the significant regression coefficients. By the same reasoning consideration of a model including more pairs differing in the valence states of Fe and Ti is not warranted at the present time.

Table 10
Regression Analysis of Optical Density (600 nm) of α-Al_2O_3: (Fe, Ti).

Type of regression[a])	rss[b])	F-Test[c])			
1. Linear terms only		1.20	ref		
2. Linear terms plus bilinear terms		0.406	yes	ref	
3. Complete second order		0.255	yes	no	ref
4. No bilinear terms		0.257	yes	no	no

[a]) c.f. equation (22).
[b]) Residual sum of squares.
[c]) Level of significance = 0.95; ref, yes and no denote reference sample, significantly different and non significantly different variances, respectively (within a column).

The fact, that the typical spectrum of (Fe, Ti) sapphire has not been observed with α-Al_2O_3:Fe and α-Al_2O_3:Ti even at high dopant concentration indicates that the biparticles (Fe, Fe) and (Ti, Ti) were not relevant and the pair (Fe, Ti) must have been responsible for the 565 and 700 nm VIS band. As a model for this particle one may suggest:

(i) In the reduced state:

$$(\mathrm{Fe, Ti})^{+6}(c, c, \mathrm{Al_2O_3}), \frac{1}{3}\,\mathrm{VAl}^{+3}(c, \mathrm{Al_2O_3}), \mathrm{H}^{+}(\mathrm{Al_2O_3})\ . \tag{23'}$$

(ii) In the oxidized state:

$$(\mathrm{Fe, Ti})^{+7}(c, c, \mathrm{Al_2O_3}), \frac{1}{3}\,\mathrm{VAl}^{+3}(c, \mathrm{Al_2O_3})\ . \tag{23''}$$

(iii) For the redox process:

$$(\mathrm{Fe, Ti})^{+7}(c, c, \mathrm{Al_2O_3}) + \frac{1}{2}\,\mathrm{H_2}(g) \rightarrow (\mathrm{Fe, Ti})^{+6}(c, c, \mathrm{Al_2O_3}) + \mathrm{H}^{+}(\mathrm{Al_2O_3})\ , \tag{23'''}$$

$$(\mathrm{Fe, Ti})^{+6}(c, c, \mathrm{Al_2O_3}) + \frac{1}{4}\,\mathrm{O_2}(g) + \mathrm{H}^{+}(\mathrm{Al_2O_3}) \rightarrow (\mathrm{Fe, Ti})^{+7}(c, c, \mathrm{Al_2O_3}) + \frac{1}{2}\,\mathrm{H_2O}(g)\ . \tag{23''''}$$

Further support for the model (22') was derived from infrared spectra and change of Fe^{+3} concentration on reduction (cf. section 3). The similarity of infrared spectra of α-Al_2O_3:Ti and α-Al_2O_3:(Fe, Ti) shows that the defect structure ((Al^{+3})-vacency)

should have been the same in both cases in accordance with models (16) and (22). By quantitative ESR intensity measurements it was found that the change of the Fe^{+3} concentration upon reduction approximately corresponded to the Ti concentration in α-Al_2O_3:(Fe, Ti). Together with the fact that no Ti^{+3} could be detected in α-Al_2O_3:(Fe, Ti) in the reduced state, this indicates that all Ti present was involved in the biparticle formation. For the electronic state of the particle (Fe, Ti) (c, c) one further statement is possible owing to the fact, that in the oxidized state Fe^{+3} and Ti^{+4} were present. For its reduced state several electronic structures may be considered possible, described by valence structures ((Fe(II), Ti(IV)), (Fe(III), Ti(III)) in resonance. In this resonance electron bands introduced by the defects in the α-Al_2O_3 electron band structure may have been involved.

5. Conclusion and Summary

A few concluding remarks concerning the system α-Al_2O_3:(Fe, Ti) seem to be in order. Though at present no direct theoretical study concerning the properties of the pair particle (Fe, Ti) are available, the results found in this work yield strong evidence for its existence and its behaviour under high temperature redox conditions. It yields a physical interpretation of the problem of non additivity of colours of transition metal ion doped sapphire. The nature of chemical bonding respresents an interesting problem, since, as may be concluded from the remarkable change in the optical spectra of the constitutents, the Fe-Ti interaction should be similar to that in charge transfer complexes or a weakly binding diatomic molecule in a strong crystal field. Very probably the interaction is particularly strong in the reduced state.

Besides biparticle formation the system α-Al_2O_3:(Fe, Ti) may be considered as a counter part to the systems α-Al_2O_3:Ni and α-Al_2O_3:Co. Though in both cases the redox process of the transition metal ion is described by equation (1), the accompanying charge compensation process leads to differently structured OHO^{-3}. Originally it was believed, that the process by which the proton is inserted into the Al_2O_3 structure is the same for all substitutable transition metal ions undergoing redox reactions in close analogy to the formation of H_3O^+ in aqueous solutions. Surprisingly this seems not to be the case however. No explanation of this phenomenon can be offered at present, though one may suppose that both the ionic radii and covalence may be responsible for it.

Acknowledgement

We should like to express our gratitude to Djevahirdjian S.A., Monthey, Switzerland, for kindly supplying samples, assistance in growing appropriate crystals and many helpful discussions. Dr. Wyttenbach from the Federal Reactor Institute (EIR) gave valuable assistance to this work by carrying out numerous neutron activation analysis. Also we enjoyed efficient support for X-ray microprobe trace analysis and free access to the instrument by Mr. Esenwein from the Federal Material Testing Institute (EMPA). One of us (K. Eigenmann) wishes to thank the Aluminium Fonds

Neuhausen, Switzerland, for a stipend. Finally generous grant of free computer time by the ETH computing center and assistance with programs by Mr. J. Keller is gratefully acknowledged.

REFERENCES

[1] D. S. McClure, J. Chem. Phys. *36*, 2257 (1962).
[2] S. Geschwind and J. P. Remeika, J. appl. Phys. Suppl. *33*, 370 (1962).
[3] M. D. Sturge, Phys. Rev. *130*, 639 (1963).
[4] J. Lambe and Ch. Kikuchi, Phys. Rev. *118*, 71 (1960).
[5] R. H. Hoskins and B. H. Soffer, Phys. Rev. *133*, A 490 (1964).
[6] S. Geschwind, P. Kislink, J. P. Remeika and D. L. Wood, Phys. Rev. *126*, 1684 (1962).
[7] M. G. Townsend and O. F. Hill, Trans. Faraday Soc. *516*, 2597 (1965).
[8] R. Müller and Hs. H. Günthard, J. Chem. Phys. *44*, 365 (1965).
[9] K. Hauffe and D. Hoeffgen, Ber. Bunsenges. physik. Chem. *74*, 537 (1970).
[10] L. S. Kornienko and A. M. Prokhorov, J. exptl. theoret. Phys. *38*, 1651 (1960); *40*, 1594 (1961); USSR.
[11] G. Lehmann and H. Harder, Am. Miner. *55*, 98 (1970).
[12] S. V. Grum-Grschumaulo, *Crystal Spectroscopy* (Academy Nauk, USSR, Moscow 1966), p. 204.
[13] C. A. Keig, J. Cryst. Growth *2*, 356 (1968).
[14] W. J. Borer, Hs. H. Günthard and P. Balmer, Helv. phys. Acta *43*, 74, 829 (1970).
[15] A. Wyttenbach, H. E. Blum, W. J. Borer, H. K. Eigenmann and Hs. H. Günthard Anal. Chim. Acta *58*, 355 (1972).
[16] Kaesermann and Sperisen AG, Biel, Switzerland.
[17] Metals Research Ltd., Cambridge, UK.
[18] J. Sci. Instrum. *5*, 84 (1972).
[19] Karl Kurtz, Thesis No. 4600, ETH Zurich, Switzerland (1970).
[20] R. A. Frey, R. D. Werder and Hs. H. Günthard, J. Mol. Spectrosc. *35*, 260 (1970).
[21] P. E. Schmid, Hs. H. Günthard, Z. angew. Math. Phys. *17*, 404 (1966).
[22] H. R. Oppliger, P. Schmid and Hs. H. Günthard, J. Sci. Instr. *42*, 865 (1965).
[23] D. S. Thompson and J. S. Waugh, Rev. Sci. Instr. *36*, 552 (1965).
[24] C. P. Poole, Jr., *Electron Spin Resonance* (Interscience Publishers, New York 1967).
[25] B. Gächter, Thesis No. 4909, ETH Zurich, Switzerland (1972), to be published.
[26] E. L. Crow, F. A. Davis and M. W. Maxfield, *Statistics Manual* (Dover Publications, New York 1960).
[27] G. Herzberg, *Molecular Spectra and Molecular Structure* (D. van Nostrand Company, Inc., New York 1950).
[28] D. M. Dennison, Rev. modern Phys. *12*, 175 (1949).
[29] G. C. Pimentel and A. L. McClellan, *The Hydrogen Bond* (Freeman, San Francisco 1960).
[30] C. W. Nestor, *Computer Program for Hartree-Fock Wave-Functions* (Oak Ridge National Laboratory, USA.)
[31] National Bureau of Standards, Circ. 467, Atomic Energy Levels, Vol. I, II (Washington 1949–1952); B. Edlén, Mon. not. R. Soc. *144*, 391 (1969).
[32] J. C. Slater, *Quantum Theory of Atomic Structure* (McGraw Hill Book Company, Inc., New York 1960).
[33] P. R. Scharma and T. P. Das, J. Chem. Phys. *41*, 3581 (1964).
[34] Y. Tanabe and S. Sugano, J. Phys. Soc. [Japan] *9*, 653, 766 (1954).
[35] International Tables of X-Ray Crystallography *1*, 274 (1952). The Kynoch Press, Birmingham.
[36] P. Ballmer, H. Blum, W. J. Borer, K. Eigenmann and Hs. H. Günthard, Helv. phys. Acta *43*, 829 (1970).
[37] National Bureau of Standards, Circ. 500, Selected Values of Chemical Thermodynamic Properties, Part I (Washington 1961).
[38] D. S. McClure, J. Chem. Phys. *39*, 2850 (1963).
[39] H. K. Eigenmann, Thesis No. 4552, ETH Zurich, Switzerland (Juris-Verlag 1970).